Table 1
Loading of Gd-DTPA/m prepared with different Pt/Gd ratio.

Sample (Pt:Gd-DTPA)	Pt linker loading	Gd-DTPA loading
0:5	0%	0%
1:5	~7.2%	~1.3%
2.5:5	~12.6%	~3%
5:5	~35%	~16%
10:5	~41%	~12%

Polymer PEG-b-PAsp (DET) 12k-45DP was used, the loading was calculated by dividing the drug amount to the total amount.

$1/T_1$ (s^{-1}) of water protons per mM concentration of CAs and calculated using expression $r_1 = (1/T_1 - 1/T_{1d})/[Gd]$, where $1/T_1$ is the longitudinal relaxation rate contrast in the presence of a paramagnetic species, $1/T_{1d}$ is the longitudinal relaxation rate contrast in the absence of a paramagnetic species and [Gd] is the concentration of paramagnetic CAs (mM). The T_1 values of Gd-DTPA, Gd-DTPA/m, or Gd-DTPA/K$_2$PtCl$_6$ solution of different Gd-DTPA/Pt ratios were measured at 37 °C in water or PBS buffer with a 0.59 T ^{1}H NMR analyzer (JNM-MU25A, JEOL) with a standard inversion-recovery pulse sequence.

2.8. Kinetic stability of Gd-DTPA/m

The stability of Gd-DTPA/m micelles under physiologic conditions was determined by DLS and static light scattering using Zetasizer Nano ZS90 (Malvern Instruments Ltd., UK). Changes of scattering light intensity were measured at defined time periods. A decrease in the scattering light intensity was associated with a decrease in the apparent molecular weight of the micelles and drug density inside the micelle core as well as in the micelle concentration. The size distribution and diameter of the Gd-DTPA/m were simultaneously monitored. The zeta-potential of Gd-DTPA/m was measured in phosphate buffer (10 mM) at pH 7.4 using Zetasizer Nano ZS90.

2.9. In vitro cytotoxicity evaluation

The cytotoxicity of Gd-DTPA/m against HUVEC and B16-F10 cell lines were evaluated by the CCK-8 assay. HUVEC and B16-F10 cells (5000 cells) were cultured with EGM-2 bullet kit and DMEM (containing 10% FBS), and then placed in 96-well plates, respectively. The cells were then exposed to Gd-DTPA, PEG-b-PAsp(DET), K$_2$PtCl$_6$ and Gd-DTPA/m for 72 h under 5% CO$_2$ at 37 °C. The Kit-8 solution was added, and followed by incubation under 5% CO$_2$ at 37 °C for 2.5 h. The absorbance at 450 nm of the produced WST-8 formazan in each well was measured using a using a micro-plate reader (Model 680, Bio-rad).

2.10. Cancer models

CDF$_1$ mice (female, 6 weeks old) were inoculated subcutaneously with C-26 cells (1 × 10^6 cells/mL). In vivo biodistribution, elemental mapping and MRI studies were performed when tumors were approximately 50 mm^3 in volume.

2.11. Biodistribution of Gd-DTPA/m

Gd-DTPA or Gd-DTPA/m was intravenously injected to the C-26 bearing mice at a dose of 78 μg/mouse on a Gd-DTPA basis. The mice were sacrificed after defined time periods (1, 4, 8 and 24 h). Tumors, livers, kidneys and spleens were excised. Blood was collected from the inferior vena cava, heparinized and centrifuged to obtain the upper plasma. Tissue samples were washed in PBS and weighed after removing excess fluid. The samples were dissolved in 90% HNO$_3$ and evaporated to dryness. The Pt and Gd concentrations were then measured by ICP-MS after the dried samples were dissolved in 1% HNO$_3$. The area under the curve (AUC) of a plot of liver, kidney, tumor and spleen drug concentration versus time was measured based on the trapezoidal rule up to 24 h after administration. Then, AUC ratios of tumor to liver, kidney and spleen are calculated.

2.12. Histology study

Mice bearing C-26 tumors were intravenously injected with Gd-DTPA/m at 100 μg/mouse on a Gd-DTPA basis. Twenty-four hours later, tumors were collected and immediately frozen in an acetone/dry ice mixture. The frozen samples were further sectioned at 6-μm thickness in a cryostat. Then, these thin sections were placed on glass slides, dehydrated in xylene and dehydrated with graded alcohols. These slides were stained with hematoxylin and eosin (H&E) and then samples were observed by using an AX80 microscope (Olympus, Japan).

2.13. In vivo MRI of Gd-DTPA/m

Solutions containing 0.2, 0.3, 0.4 and 0.5 mM Gd-DTPA or Gd-DTPA/m were placed in thin-wall PCR tubes, and then closed with flat caps for MR imaging at 1 T (Aspect, Aspect Imaging) and 7 T (BioSpec 70/20USR, Bruker). In vivo MR images were obtained using 1 T imaging spectrometer. For the T_1-weighted images of the mice, the following parameters were adopted: spin-echo method, repetition time (TR) = 400 ms, echo time (TE) = 11 ms, field of view (FOV) = 48 × 48 mm, matrix size = 256 × 256, and slice thickness = 2 mm. MR images were obtained from C-26 tumor bearing mice when the mean tumor volume was 100 mm^3. For all of the mice, transaxial T_1-weighted images were taken before injecting Gd-DTPA/m or Gd-DTPA as a control imaging. The mice were anesthetized with 1.8% isoflurane during the MRI experiments. The mice were injected i.v. with 0.22 mmol/kg of Gd-DTPA alone or 0.02 mmol/kg of Gd-DTPA/m based on Gd-DTPA. The transaxial T1W images were taken with a phantom containing water as a reference signal in defined time. The images were reconstructed and analyzed using ParaVision (Bruker Biospin) and Image J (NIH).

2.14. Element analysis using μ-SR-XRF

Micro-synchrotron radiation-induced X-ray fluorescence spectrometry imaging (μ-SR-XRF) was used to determine Gd-DTPA as well as Fe, Pt distribution in sections of solid tumor. Briefly, CDF$_1$ mice bearing C-26 tumor were intravenously injected with Gd-DTPA/m at 100 μg/mouse on a Gd-DTPA basis. Twenty-four hours later, tumors were collected and immediately frozen in acetone/dry ice, and then sliced using a cryostat and fixed on polypropylene sheets. μ-SR-XRF was performed using
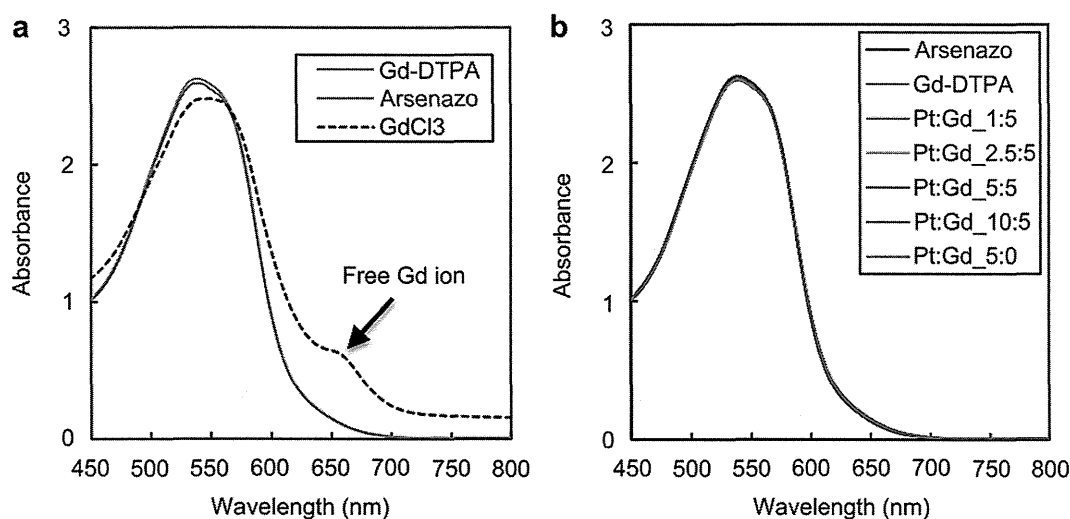

Fig. 2. Absorption spectrum of Arsenazo(III) solution with different mole ratios of Gd-DTPA and K$_2$PtCl$_6$ mixture solutions, the concentration of Gd-DTPA was maintained at 5 mM, the Pt concentration increased from 0 to 10 mM. The mixture of K$_2$PtCl$_6$ with Gd-DTPA did not compromise the stability of Gd-DTPA chelate.
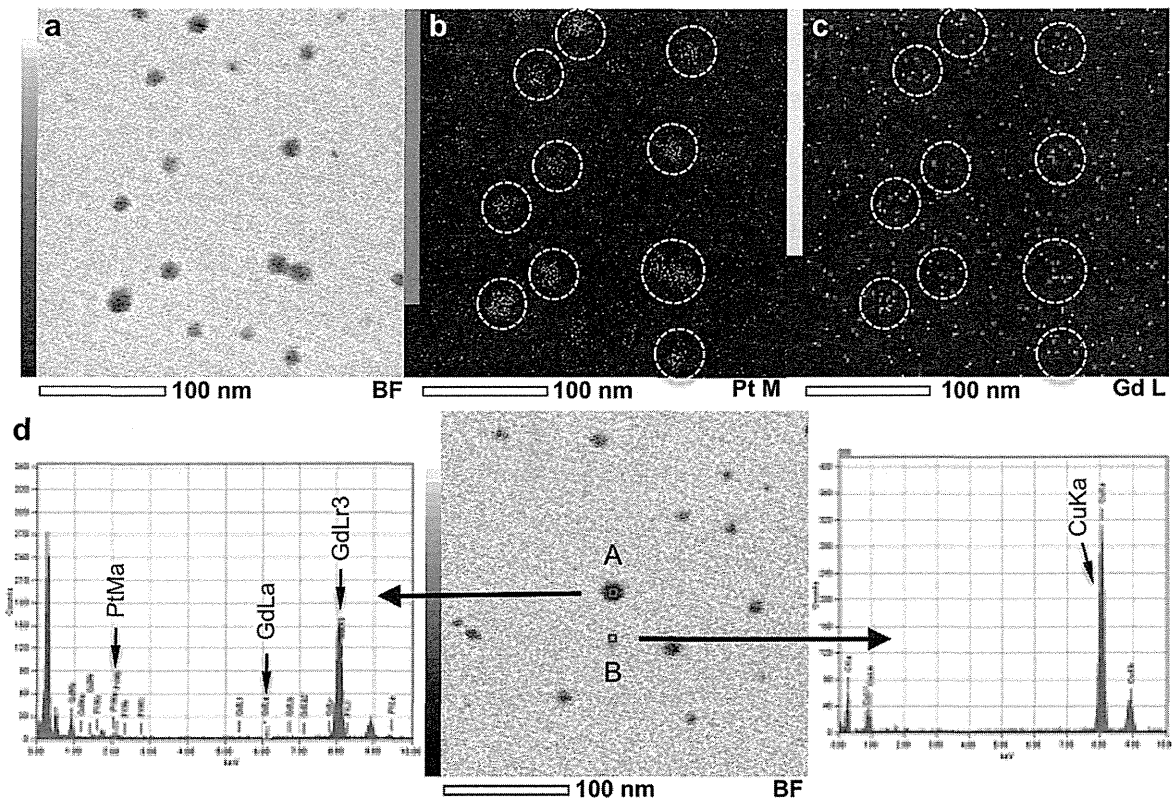
Fig. 3. EDS analysis of Gd-DTPA/m. (a) STEM image of Gd-DTPA/m. (b) Pt distribution under the STEM pattern. (c) Gd distribution under the STEM pattern. (d) EDX spectra of Gd-DTPA/m and background.

beam line 37XU at SPring-8 (Hyogo, Japan), operated at 8 GeV and ~100 mA. A photon beam with 14 keV of energy, a beam spot size of 1.3 × 1.3 μm², and an intensity of 1 × 10¹² photons/s was used to irradiate the tissue sample. The fluorescence X-rays were measured using a Si-SSD in air at room temperature. Each sample on the acryl board was mounted on an x–y translation stage. The fluorescence X-ray intensity was normalized by the incident X-ray intensity, I_0, to produce a two-dimensional elemental map. An area of 250 × 250 μm² of the tissue sections was roughly scanned before μ-SR-XRF imaging.

3. Results and discussion

PEG-b-PAsp(DET) copolymers with different degree of polymerization (DP) (DP = 25, 35 and 45) were synthesized by

aminolysis reaction of PEG-b-PBLA with diethylenetriamine (Scheme S1). PEG can hinder the interaction of the micelles with plasma proteins and prolong their circulation time in blood, while PAsp(DET) segments are minimally toxic and biodegradable as PAsp main-chain is fragmented from the nucleophilic attack of DET side chain via the formation of a succinimide ring [32]. Pt(IV) could form very stable chelates with amino groups of ethylenediamine and labile complexes with carboxylic groups [19,33]. Thus, as K_2PtCl_6 were mixed with PEG-b-PAsp(DET) and Gd-DTPA in aqueous solution, the block copolymers self-assembled into core–shell polymeric micelles carrying Gd-DTPA in the core as shown in Scheme 1. The K_2PtCl_6 concentration was found to be critical for the
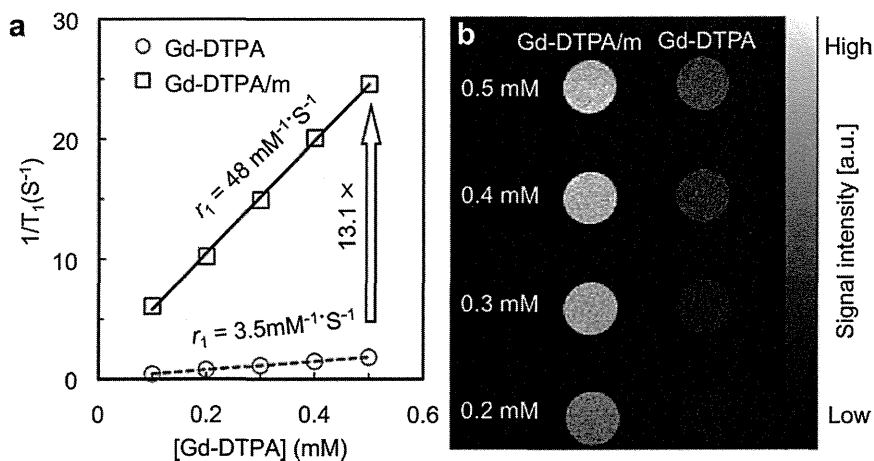

Fig. 4. MR enhancement effect of Gd-DTPA/m. (a) T_1 relaxivity coefficient. (b) T_1 weight MR images of Gd-DTPA/m and free Gd-DTPA solutions at 1 T.
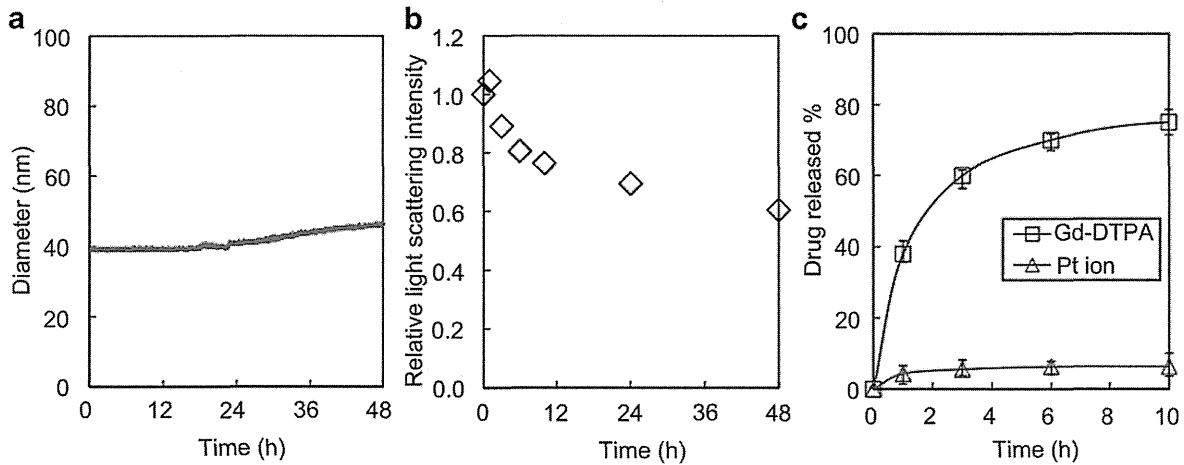
Fig. 5. Physicochemical characterization of Gd-DTPA/m under physiologic conditions. (a) Real time changes of diameter and (b) Change in relative light scattering intensity of Gd-DTPA/m. (c) Release rate of Gd-DTPA and Pt complexes from Gd-DTPA/m under similar conditions.

formation of micelles as without K_2PtCl_6, or even at low K_2PtCl_6 concentration, the micelles did not assemble (Fig. 1a and b). At 5 and 10 mM of K_2PtCl_6, narrowly distributed micelles were formed incorporating 16% and 12% of Gd-DTPA in weight, respectively (Table 1). Besides, the micelles prepared with PEG-*b*-Asp(DET) having longer PAsp(DET) segments showed higher loading of Gd-DTPA (DP = 45, 16%) than those PAsp(DET) with shorter segments

(8% for DP = 25, and 9% for DP = 35) as shown in Table S1. Therefore, we decided to use Gd-DTPA/m prepared from PEG-*b*-PAsp(DET) (DP = 45), 5 mM Gd-DTPA and 5 mM K_2PtCl_6 for all of the following experiments as this composition produced micelles with highest Gd-DPTA loading. In addition, we confirmed that K_2PtCl_6 did not break the Gd-DTPA chelates as Gd^{3+} was not detectable, by arsenazo III method [31], at any ratio of Gd-DTPA/K_2PtCl_6 (Fig. 2).
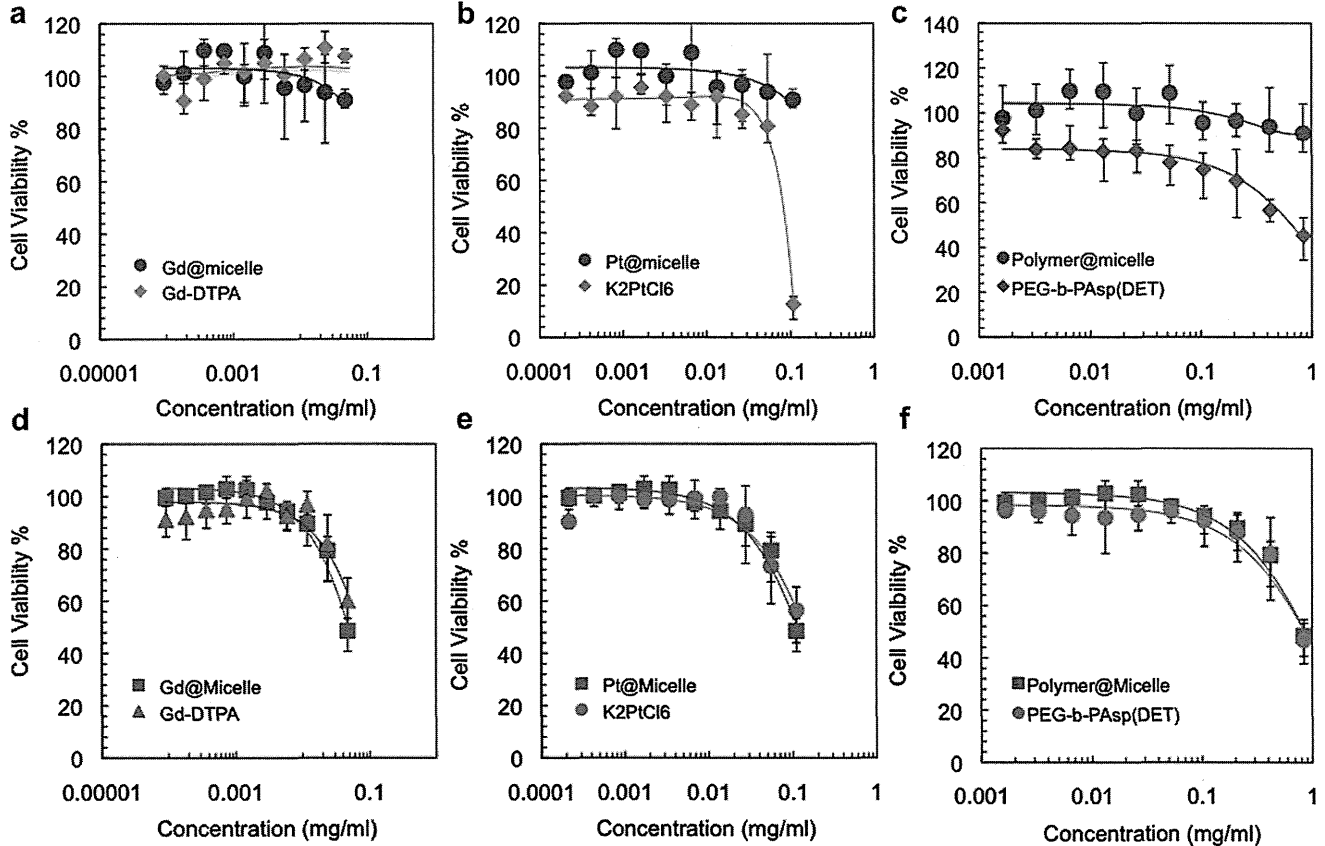

Fig. 6. Cytotoxicity of Gd-DTPA/m against HUVEC (a–c) and murine melanoma B16-F10 cells (d–f) after 72 h incubation. Micelles show comparable or even higher cell viability than free components, i.e., Gd-DTPA, K_2PtCl_6 and PEG-*b*-PAsp(DET).

The z-average diameter by intensity of these micelles was approximately 45 nm according to dynamic light scattering (Fig. 1c), and their zeta-potential was close to neutral at pH 7.4 (Figure S5). Diameter of sub-50 nm nanocarriers is important to achieve their deep tumor penetration in poorly permeable tumors according to our recent study [34]. Thus, the size of Gd-DTPA/m may be suitable for MR imaging of solid tumors with reduced permeability. According to TEM, Gd-DTPA/m showed quite narrowly distributed spherical morphology (Fig. 1d, e and Figure s6). Accordingly, the average size of the Gd-DTPA/m was calculated to be 22 nm (Fig. 1f), which is consistent with the number-averaged distribution (23 nm) calculated from z-averaged data obtained by DLS.

The elemental mapping under scanning TEM (STEM) and energy dispersive X-ray spectroscopy (EDS) of Gd-DTPA/m (Fig. 3) proved the existence of Gd and Pt elements inside the core of micelles. These results correlate with ICP-MS data (Table 1) as Pt concentration is higher than Gd encapsulated inside micelle.

The relaxivity of Gd-DTPA/m increased to 48 $mM^{-1}\,s^{-1}$ based on Gd-DTPA, which is approximately 13-fold higher than that of free Gd-DTPA (Fig. 4a). T_1-weighted spin echo MRI at 1 T also revealed that Gd-DTPA/m highly improved MR contrast enhancement
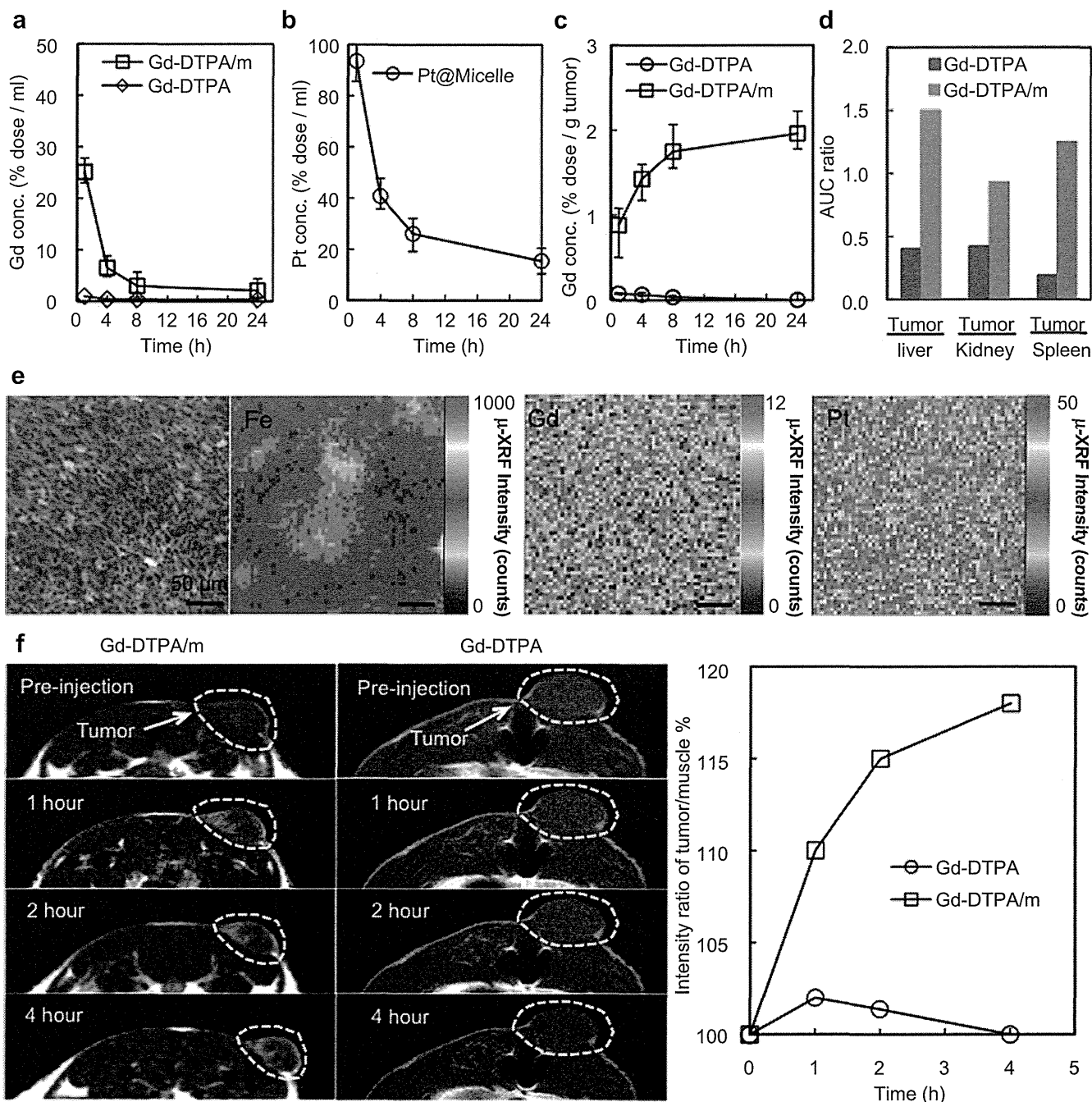

Fig. 7. In vivo evaluation of Gd-DTPA/m. (a) Plasma clearance of Gd-DTPA/m and free Gd-DTPA. (b) Plasma clearance of Pt@micelles. (c) Tumor accumulation of Gd-DTPA/m and free Gd-DTPA. (d) Tumor to tissue AUC ratios. (e) Microscopic findings (H&E staining) of tumor tissue and element distribution in tumor section. (f) T_1 weight tumor contrast enhancement after i.v. injection of Gd-DTPA loaded micelle and free Gd-DTPA.

499

compared to free Gd-DTPA (Fig. 3b), which may be attributed to a prolongation of the rotational correlation time, τ_R, due to restricted local motion similar to that of Gd-DTPA bound to macromolecules [35]. The benefits of slow rotation are observed at lower field strengths as the prevailing correlation time is almost always rotational diffusion, while at higher magnetic fields, the relaxivity of these Gd^{3+} complexes immobilized on slowly tumbling macromolecules rapidly decreases [36–38]. Accordingly, T_1-weighted spin echo MRI at 7 T showed that the contrast of Gd-DTPA/m was similar to free Gd-DTPA (Figure S7). Since clinical MRI machines use magnetic fields as high as 1.5 T, the design of Gd-DTPA/m is suitable for high relaxivity contrast enhancement at low dose. Interestingly, r_1 of Gd-DTPA/m augmented as the Pt/Gd ratio inside the core increased (Figure S8). Conversely, the r_1 relaxivity of Gd-DTPA/K_2PtCl_6 mixtures at different mole ratios or incubation time showed no significant r_1 relaxivity enhancement (Figure S9) suggesting that the incorporation of Gd-DTPA in the micelles core is necessary for the enhancement of relaxivity.

The micelles were stable under physiological conditions, i.e. in 10 mM PBS (pH 7.4) with 150 mM NaCl at 37 °C. In physiological environments, the diameter of the micelles slightly augmented after 18–20 h (Fig. 5a). Moreover, 60% of the initial light scattering intensity of the micelles was detectable even after 48 h (Fig. 5b). During the exposure of the micelles to physiological conditions, 75% Gd-DTPA was released in approximately 10 h, while only 7% of Pt was released probably due to stable metal complexation of Pt(IV) with PEG-b-PAsp(DET) (Fig. 5c). The ability of Gd-DTPA/m to sustainedly release Gd-DTPA, which can undergo glomerular filtration in the kidneys, may reduce the risk of free Gd discharge in the body.

Gd-DTPA/m was not cytotoxic against both primary cell lines (HUVEC) and tumor cell lines (B16-F10) (Fig. 6), suggesting its safety for in vivo application. Gd-DTPA/m extended the circulation of Gd-DTPA in the bloodstream, attaining 5% of the injected dose of Gd-DTPA after 8 h, while free Gd-DTPA was rapidly cleared from plasma (Fig. 7a and b). Moreover, approximately 15% of the injected Pt remained in the bloodstream after 24 h, which indicates the circulation of the micelles in the bloodstream. Gd-DTPA/m was able to deliver 26-fold higher CA in subcutaneous murine colon adenocarcinoma 26 (C-26) than free Gd-DTPA (Fig. 7c). In addition, the ratio of AUC in tumor versus organs indicated that Gd-DTPA/m improved the tumor-to-organ distribution of Gd-DTPA (Fig. 7d).

The microdistribution of the drugs at the tumor site was studied by micro-synchrotron radiation-induced X-ray fluorescence spectrometry imaging (μ-SR-XRF) of the tumor sites as Pt and Gd showed very distinct peaks in the sum spectrum of the line scan. Moreover, Fe mapping was also evaluated as it characterizes hemeproteins and therefore the positioning of blood vessels in the tissue. The atoms of Gd as well as Pt located in the whole tumor section in areas far from the Fe-rich regions suggesting deep tumor penetration and accumulation of Gd-DTPA/m as shown in Fig. 7e, in which the rainbow scales represent the quantity of element.

The size, neutral surface charge, stability and release characteristics of Gd-DTPA/m may contribute to the high penetration and accumulation of Gd-DTPA at the tumor site. The higher tumor accumulation and higher relaxivity of Gd-DTPA/m clearly and selectively enhanced the contrast at the tumor area in T_1-weighted MR images, even at low dose (0.02 mmol/kg based on Gd-DTPA) of contrast agents (Fig. 7f). The tumor selective contrast enhancement of Gd-DTPA/m was significant from 1 h after injection until the end of the experiment, that is, 4 h after injection. Oppositely, intravenously injected free Gd-DTPA, even at a 10 times higher dose, that is, 0.22 mmol/kg, failed to increase the intensity of the signal in the tumor region. These findings indicate the potential of GD-DTPA/m as a tumor-selective contrast agent.

4. Conclusion

Gd-DTPA/m efficiently improved the MRI-contrast of solid tumors demonstrating its potential application in the bio-imaging field. Accordingly, the sub-50 nm size, neutral surface and biological stability of Gd-DTPA/m, and the increased relaxivity of Gd-DTPA in the core of micelles lead to selective contrast enhancement of tumors. This facile and reversible metal complexation used for the construction of Gd-DTPA/m could also be applied for incorporating hydrophilic imaging probes, therapeutic drugs, or bioactive molecules into nanodevices for diagnosis and therapy. Accordingly, here, we illustrated a new approach for designing nano-sized vehicles by incorporating drugs via metal complexation besides widely used methods, such as covalent conjugation, or hydrophobic interaction, demonstrating its further application for loading compounds, which are difficult to incorporate in traditional nanocarriers.

Appendix A. Supplementary data

Supplementary data related to this article can be found at http://dx.doi.org/10.1016/j.biomaterials.2012.09.030.

References

[1] Weissleder R, Pittet MJ. Imaging in the era of molecular oncology. Nature 2008;452:580–9.
[2] Mansfield P. Snapshot magnetic resonance imaging. Angew Chem Int Ed 2004; 43:5456–64.
[3] Weinmann HJ, Brasch RC, Press WR, Wesbey GE. Characteristics of gadolinium-DTPA complex: a potential NMR contrast agent. AJR Am J Roentgenol 1984; 142:619–24.
[4] Davis PL, Kaufman L, Crooks LE, Miller TR. Detectability of hepatomas in rat livers by nuclear magnetic resonance imaging. Invest Radiol 1981;16:354–9.
[5] Laurent S, Elst LV, Muller RN. Comparative study of the physicochemical properties of six clinical low molecular weight gadolinium contrast agents. Contrast Media Mol Imaging 2006;1:128–37.
[6] Ananta JS, Godin B, Sethi R, Moriggi L, Liu XW, Serda RE, et al. Geometrical confinement of gadolinium-based contrast agents in nanoporous particles enhances T-1 contrast. Nat Nanotech 2010;5:815–21.
[7] Thompson KH, Orvig C. Boon and bane of metal ions in medicine. Science 2003;300:936–9.
[8] Ferrari M. Cancer nanotechnology: opportunities and challenges. Nat Rev Cancer 2005;5:161–71.
[9] Cabral H, Nishiyama N, Kataoka K. Supramolecular nanodevices: from design validation to theranostic nanomedicine. Acc Chem Res 2011;44:999–1008.
[10] Kataoka K, Harada A, Nagasaki Y. Block copolymer micelles for drug delivery: design, characterization and biological significance. Adv Drug Deliv Rev 2001; 47:113–31.
[11] Nishiyama N, Morimoto Y, Jang WD, Kataoka K. Design and development of dendrimer photosensitizer-incorporated polymeric micelles for enhanced photodynamic therapy. Adv Drug Deliv Rev 2009;61:327–38.
[12] Rafi M, Cabral H, Kano MR, Mi P, Iwata C, Yashiro M, et al. Polymeric micelles incorporating (1,2-diaminocyclohexane)platinum (II) suppress the growth of orthotopic scirrhous gastric tumors and their lymph node metastasis. J Control Release 2012;159:189–96.
[13] Mikhaylov G, Mikac U, Magaeva AA, Itin VI, Naiden EP, Psakhye I, et al. Ferri-liposomes as an MRI-visible drug-delivery system for targeting tumours and their microenvironment. Nat Nanotech 2011;6:594–602.

[14] Floyd III WC, Klemm PJ, Smiles DE, Kohlgruber AC, Pierre VC, Mynar JL, et al. Conjugation effects of various linkers on Gd(III) MRI contrast agents with dendrimers: optimizing the hydroxypyridinonate (HOPO) ligands with nontoxic, degradable esteramide (EA) dendrimers for high relaxivity. J Am Chem Soc 2011;133:2390–3.

[15] Kojima C, Turkbey B, Ogawa M, Bernardo M, Regino CAS, Bryant LH, et al. Dendrimer-based MRI contrast agents: the effects of PEGylation on relaxivity and pharmacokinetics. Nanomedicine 2011;7:1001–8.

[16] Khemtong C, Kessinger CW, Ren J, Bey EA, Yang SG, Guthi JS, et al. In vivo off-resonance saturation magnetic resonance imaging of alphavbeta3-targeted superparamagnetic nanoparticles. Cancer Res 2009;69:1651–8.

[17] Mulder WJM, Strijkers GJ, van Tilborg GAF, Griffioen AW, Nicolay K. Lipid-based nanoparticles for contrast-enhanced MRI and molecular imaging. NMR Biomed 2006;19:142–64.

[18] Ai H. Layer-by-layer capsules for magnetic resonance imaging and drug delivery. Adv Drug Deliv Rev 2011;63:772–88.

[19] Vucic E, Sanders HM, Arena F, Terreno E, Aime S, Nicolay K, et al. Well-defined, multifunctional nanostructures of a paramagnetic lipid and a lipopeptide for macrophage imaging. J Am Chem Soc 2009;131:406–7.

[20] Kaida S, Cabral H, Kumagai M, Kishimura A, Terada Y, Sekino M, et al. Visible drug delivery by supramolecular nanocarriers directing to single-platformed diagnosis and therapy of pancreatic tumor model. Cancer Res 2010;70:7031–41.

[21] Nasongkla N, Bey E, Ren JM, Ai H, Khemtong C, Guthi JS, et al. Multifunctional polymeric micelles as cancer-targeted, MRI-ultrasensitive drug delivery systems. Nano Lett 2006;6:2427–30.

[22] Yokoyama M, Nakamura E, Makino K, Okano T, Yamamoto TA. Polymeric micelle MRI contrast agent with changeable relaxivity. J Control Release 2006; 114:325–33.

[23] Manus LM, Mastarone DJ, Waters EA, Zhang XQ, Schultz-Sikma EA, MacRenaris KW, et al. Gd(III)-nanodiamond conjugates for MRI contrast enhancement. Nano Lett 2010;10:484–9.

[24] Torchilin VP. PEG-based micelles as carriers of contrast agents for different imaging modalities. Adv Drug Deliv Rev 2002;54:235–52.

[25] Ai H, Flask C, Weinberg B, Shuai X, Pagel MD, Farrell D, et al. Magnetite-loaded polymeric micelles as ultrasensitive magnetic-resonance probes. Adv Mater 2005;17:1949–52.

[26] Duncan R, Izzo L. Dendrimer biocompatibility and toxicity. Adv Drug Deliv Rev 2005;57:2215–37.

[27] Matsumura Y, Kataoka K. Preclinical and clinical studies of anticancer agent-incorporating polymer micelles. Cancer Sci 2009;100:572–9.

[28] Plummer R, Wilson RH, Calvert H, Boddy AV, Griffin M, Sludden J, et al. A phase I clinical study of cisplatin-incorporated polymeric micelles (NC-6004) in patients with solid tumours. Br J Cancer 2011;104:593–8.

[29] Harada A, Kataoka K. Formation of polyion complex micelles in an aqueous milieu from a pair of oppositely-charged block-copolymers with poly(ethylene glycol) segments. Macromolecules 1995;28:5294–9.

[30] Kanayama N, Fukushima S, Nishiyama N, Itaka K, Jang WD, Miyata K, et al. A PEG-based biocompatible block catiomer with high buffering capacity for the construction of polyplex micelles showing efficient gene transfer toward primary cells. ChemMedChem 2006;1:439–44.

[31] Gouin S, Winnik FM. Quantitative assays of the amount of diethylene-triaminepentaacetic acid conjugated to water-soluble polymers using isothermal titration calorimetry and colorimetry. Bioconjug Chem 2001;12: 372–7.

[32] Itaka K, Ishii T, Hasegawa Y, Kataoka K. Biodegradable polyamino acid-based polycations as safe and effective gene carrier minimizing cumulative toxicity. Biomaterials 2010;31:3707–14.

[33] Iakovidis A, Hadjiliadis N. Complex-compounds of platinum(II) and platinum(IV) with amino-acids, peptides and their derivatives. Coord Chem Rev 1994;135:17–63.

[34] Cabral H, Matsumoto Y, Mizuno K, Chen Q, Murakami M, Kimura M, et al. Accumulation of sub-100nm polymeric micelles in poorly permeable tumours depends on size. Nat Nanotech 2011;6:815–23.

[35] Caravan P, Ellison JJ, McMurry TJ, Lauffer RB. Gadolinium(III) chelates as MRI contrast agents: structure, dynamics, and applications. Chem Rev 1999;99: 2293–352.

[36] Terreno E, Castelli DD, Viale A, Aime S. Challenges for molecular magnetic resonance imaging. Chem Rev 2010;110:3019–42.

[37] Mastarone DJ, Harrison VSR, Eckermann AL, Parigi G, Luchinat C, Meade TJ. A modular system for the synthesis of multiplexed magnetic resonance probes. J Am Chem Soc 2011;133:5329–37.

[38] Caravan P, Farrar CT, Frullano L, Uppal R. Influence of molecular parameters and increasing magnetic field strength on relaxivity of gadolinium- and manganese-based T1 contrast agents. Contrast Media Mol Imaging 2009;4: 89–100.

research article

Assessing renal function in children with hydronephrosis - additional feature of MR urography

George Hadjidekov[1,2], Savina Hadjidekova[3], Zahari Tonchev[1,2], Rumiana Bakalova[2,4], Ichio Aoki[4]

[1] Department of Radiology, University Hospital "Lozenets", Sofia, Bulgaria
[2] Department of Physics, Biophysics & Radiology, Medical Faculty, University Sofia University "St. Kl. Ohridski", Sofia, Bulgaria
[3] Department of Medical Genetics, Medical University, Sofia, Bulgaria
[4] Molecular Imaging Center, National Institute of Radiological Sciences (NIRS), Chiba, Japan.

Background. Magnetic resonance urography (MRU) is one of the most attractive imaging modalities in paediatric urology, providing largest diagnostic information in a single protocol. Therefore, the aim of our study was to assess the diagnostic value of MRU in children with urogenital anomalies (especially anomalies of the renal pelvis and ureter) and the renal function using different post-processing functional software.

Patients and methods. Ninety six children (7 days – 18 years old) were examined. In 54 patients of them, a static T_2 MRU was completed by excretory T_1 MRU after gadolinium administration and functional analysis has been performed using two functional analysis softwares "CHOP-fMRU" and "ImageJ" software.

Results. MRU showed suspicious renal and the whole urinary tract anomalies with excellent image quality in all children. In ureteropelvic obstruction, MRU was confirmatory to the other imaging techniques, but it was superior modality concerning the evaluation of end-ureteral anomalies. There was an excellent correlation between the MRU data and diagnosis, determined by surgery. The renal transit times, renal volumes and volumetric differential renal function were assessed separately by "CHOP-fMRU" and "ImageJ" with excellent agreement with 99^{m}Tc-DTPA and among them.

Conclusions. MRU overcomes a lot of limitations of conventional imaging modalities and has a potential to become a leading modality in paediatric uroradiology. Synthesis of both anatomical and functional criteria in MR urography enables to select the best candidates for surgical treatment. Even small kidney dysfunction can be detected by functional analysis software.

Key words: MR urography; children; functional analysis; urinary tract

Introduction

The imaging of urinary tract is important clue in paediatrics. Different methods for evaluation of the genitourinary system are routinely used in the clinic. However, there is no single method providing the whole information, necessary for the diagnostic. The conventional methods have many limitations. For example: ultrasound examination is operator-dependant, with sometimes difficult visualization of the end-ureter; in intravenous urography, there is a risk of contrast media and ionizing radiation; retrograde methods are invasive with limited application; scintigraphy has a poor anatomical resolution.[1]

Novel methods have developed to overcome the limitations of the conventional methods and MR urography (MRU) is one of the most attractive. MRU is a promising method for early diagnosis, having an impact on the management of congenital malformations and other urogenital anomalies in children.[1] This diagnostic modality provides a detailed visualization of various morphologic abnormalities of the genitourinary system and avoids

radiation, which is mutagenic.[1,2] To avoid ionizing radiation is one of the most important diagnostic approaches in children.[3]

Currently, MRI is used in paediatrics for assessment of the congenital abnormalities of the genitourinary system, different cases of obstruction of the excretory system and evaluation of renal tumours, which are prevalent solid tumours in infants.[1,4] In addition to the morphological imaging, MRI can be used to quantify the renal function. Following contrast administration and using appropriate software, time-intensity curves can be generated and other parameters (e.g., renal transit times, renal volumes and differential renal function) can be quantified.[1] This is the reason some authors to define MRI as a potential "one-stop-shop" imaging technique for a variety of renal diseases.[6-8]

In the present study, we assess the diagnostic value of MRU in a cohort of paediatric patients with various urogenital anomalies (especially with anomalies of the renal pelvis and ureter) using two post-processing functional software "CHOP-fMRU" and ImageJ and in comparison to 99mTc-DTPA scintigraphy.

Materials and methods

Patient population

We retrospectively reviewed all 96 children (age: between 7 days and 18 years) referred from the Department of Urology and Paediatrics, between 2006 and 2010 with suspected congenital urinary tract anomalies, controversial findings from the conventional imaging studies and difficulties to establish the final diagnosis. In 54 of them an excretory, T_1 MRU after contrast administration of gadolinium has been performed for renal function assessment in addition to T2 MR urography. In the remaining 42 patients, static T2 MR urography has been employed in order to confirm conditions affecting the urinary tract without impact on the renal function, co-existing renal pathology or due to contraindications for gadolinium (Gd) injection in cases of renal failure. The frequency of age distribution in the patient population was as follows: 0 day – 1 month: 7 patients (7.3% from the whole study group of 96 patients); 1 month – 1 year: 29 patients (30.2%); 1 year – 6 years: 18 patients (18.8%); 6 years – 14 years: 15 patients (15.6%); 14 years – 18 years: 27 patients (28.1%).

Cross-sectional sequences, MR angiography in the arterial and venous phase, serial evaluation of the renal parenchymal perfusion and contrast-en-

hanced MRU were combined in one imaging session instead of lining up several different imaging modalities. Time-intensity curves were generated, based on the dynamic 3D post-contrast sequences. "CHOP-fMRU" and ImageJ analysis software was used for calculation the functional curves, plots and maps, renal transit times, renal volumes and differential renal function.[5,10] In all cases, an informed consent was obtained after the procedure was fully explained to the parents and older children and the study was approved by the Ethics Committee of the University Hospital "Lozenets", Sofia, Bulgaria.

Ultrasonography was conducted in all patients prior to MRU examination. Voiding cystourethrography (VCUG) was performed in 10 children with suspicion for dilatation of urinary tract in accordance to vesicoureteral reflux (VUR). In 8 children intravenous urography (IVU) has been previously done and in 19 cases 99mTc-DTPA scintigraphy as a part of the uroradiological work-up has been done with a delay prior or after the MRI exam no longer than 1 month, in another institution. The 99mTc-DTPA protocol was similar to our MRU protocol in terms of hydration with intravenous administration of 10 ml/kg sodium chloride solution 30 min prior to the scan. The amount furosemide (1 mg/kg, i.v.) was the same as in our examination, although diuretics have been given when maximum pelvicalyceal distension was observed (usually 10-15 min after administration of 99mTc-DTPA).

Patient preparation

The adequate preparation is a prerequisite for a good image quality.[5-11] We didn't place routinely a bladder catheter, although catheterisation of small children is recommended in case of megaureter (with or without reflux). We used catheter in few patients with suspected VUR, but due to technical problems we abandoned this procedure. Then we started to scan without catheterization and we were happy with cooperative, toilet-trained children, without cases of severe discomfort or inability to conduct the examination. The intravenous hydration and administration of furosemide are crucial for reducing the concentrations of Gd.[10] Diuretics are recommended in both static urography and dynamic urography before contrast administration. In this context, we administered standardised hydration (10-15 ml/kg sodium chloride or Ringer's solution) and diuretics (furosemide – 1 mg/kg, max. dose 20 mg) 15 min prior to Gd injection, in order to reduce artefacts, to distend
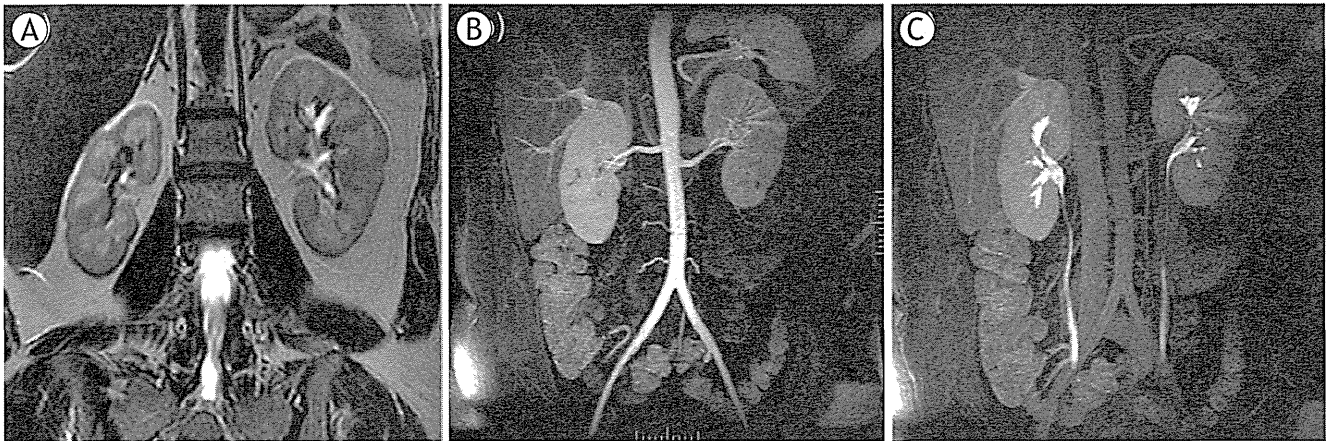
Coronal T2 native image
(without contrast probe)

MIP image in arterial phase
(post-contrast MRU)

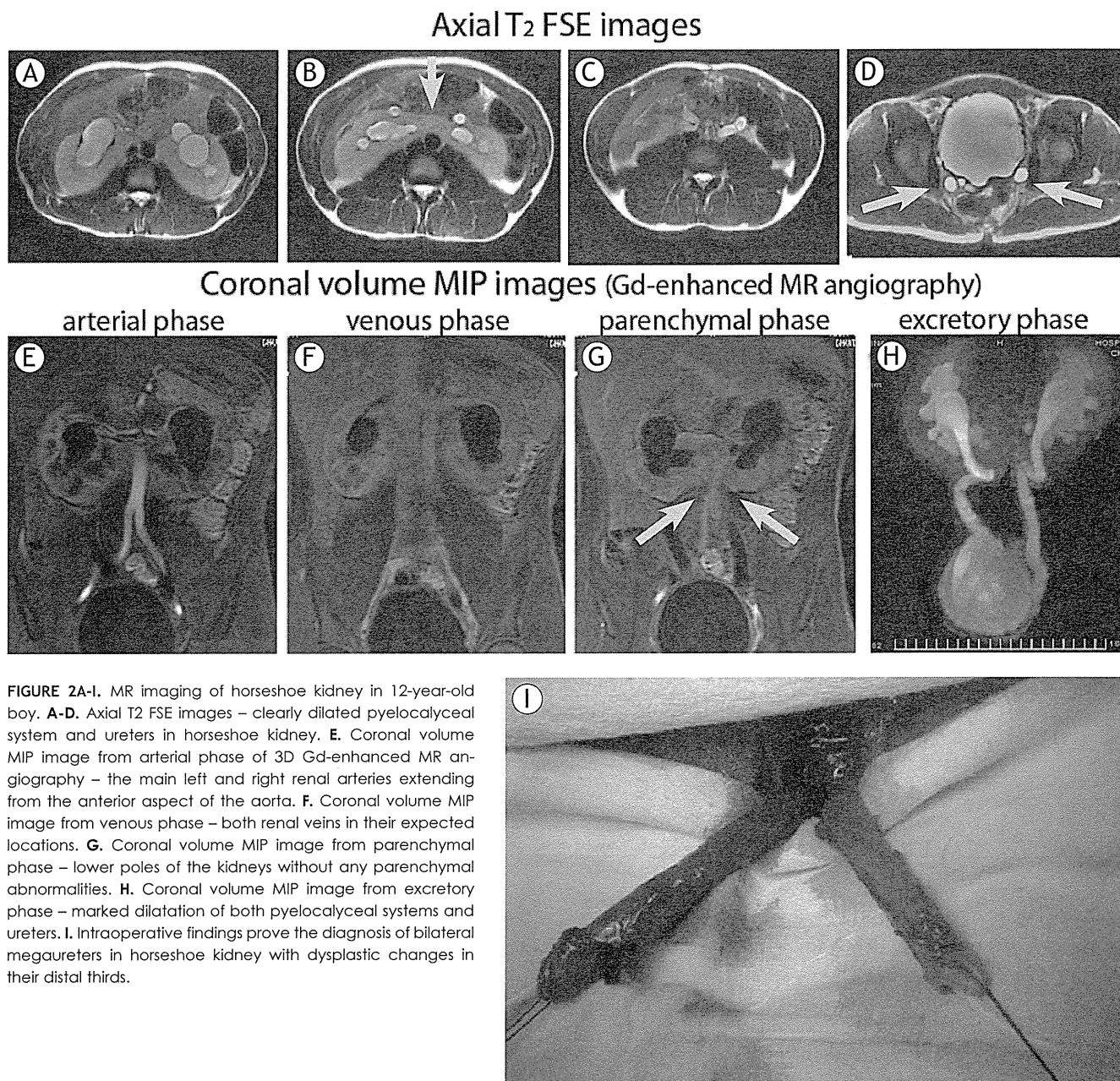## MIP image during excretion
(post-contrast MRU)

FIGURE 1A-C. Normal MR urogram in 5-year-old boy. A. Coronal T2 native image of both kidneys. B,C. MIP images from two separated time-points of the excretory post-contrast MRU in arterial phase (B) and during excretion (C).

the urinary tract, to maintain the linearity between signal intensity and concentration of Gd and to shorten the examination time, adopting the F-15 protocol, proposed by Grattan-Smith.[12] In children younger than 6-year-old and non-cooperative for breath-hold techniques, successful sedation was performed with ketamine (Ketalar) and midazolam (Dormicum) according to the department's standard sedation protocol with no serious adverse effects. In 15 patients intravenous sedation (Ketalar – 1 mg/kg or Thiopental 4-5 mg/kg) was successfully performed with minor motion artefacts in 2 infants without any impact on the diagnostic value of the image quality. Oral sedation using midazolam (Dormicum - 0.5 mg/kg) was sufficient to perform MRU with excellent diagnostic image quality in 32 patients and there was no major complaint of nausea and vomiting that could be related to antiemetic effects of midazolam.[13-14] The blood pressure, respiration, heart rate, and oxygen saturation were continuously monitored throughout MR imaging in all patients.

MRU protocol

High-field strength tomographs (1.5 Tesla) (Signa, General Electric Medical Systems and Magnetom Essenza, Siemens Medical Solutions) were used with large field of view (FOV) above diaphragm to avoid artefacts from aliasing or post-contrast signal intensity decline in the upper renal poles and obtain an oblique coronal plan angled parallel to the long axis of the kidneys, including ureters and bladder. Our MRU protocol consisted of native MR examination with T_2 coronal, T_1 and T_2 axial sequences, followed by dynamic study with Gd injection, administration of furosemide prior to the dynamic acquisitions and 3D reconstructions. Following the coronal T_2 plan, we performed axial T_2 and T_1 sequences. Fat-suppression techniques were used in T_1 and T_2 hyperintense findings and in cases of suspicion of tumour formation – In/Out phase dual-echo sequences for contour delineation. The most important pre-contrast sequence was 3D T_2 urogram with fat-suppression and respiratory-triggering. T_1-weighted gradient-echo sequence with fat-saturation (3D Dyn SPGR for GE 1.5 T Signa and 3D VIBE Dynamic for Siemens Essenza 1,5T) was used for the post-contrast scan. The dynamic scan was repeated within 15 min, following Gd injection with increasing intervals between acquisitions, for the need of post-processing. Our sequences were compatible on both MR units and the software used for post-processing has been properly validated for correctness and applicability in our MR protocols. We employed a standard dose of 0.1 mmol/kg of Gd in the majority of our studies, however in some occasions low-dose Gd opacification – 0.01 mmol/kg has been employed, especially in small infants and in cases of glomerular filtration between 30 and 60 ml/min/1.73 m². In all our patients, serum creatinine levels were strictly observed and we estimated individually the glomerular filtration rate according to the Schwartz's formula.[15] New-borns and small infants were scanned with a head-coil and the older children were scanned with a phased-array torso coil. Normal MR urogram is shown in Figure 1.

Axial T2 FSE images

Coronal volume MIP images (Gd-enhanced MR angiography)
arterial phase   venous phase   parenchymal phase   excretory phase

FIGURE 2A-I. MR imaging of horseshoe kidney in 12-year-old boy. **A-D.** Axial T2 FSE images – clearly dilated pyelocalyceal system and ureters in horseshoe kidney. **E.** Coronal volume MIP image from arterial phase of 3D Gd-enhanced MR angiography – the main left and right renal arteries extending from the anterior aspect of the aorta. **F.** Coronal volume MIP image from venous phase – both renal veins in their expected locations. **G.** Coronal volume MIP image from parenchymal phase – lower poles of the kidneys without any parenchymal abnormalities. **H.** Coronal volume MIP image from excretory phase – marked dilatation of both pyelocalyceal systems and ureters. **I.** Intraoperative findings prove the diagnosis of bilateral megaureters in horseshoe kidney with dysplastic changes in their distal thirds.

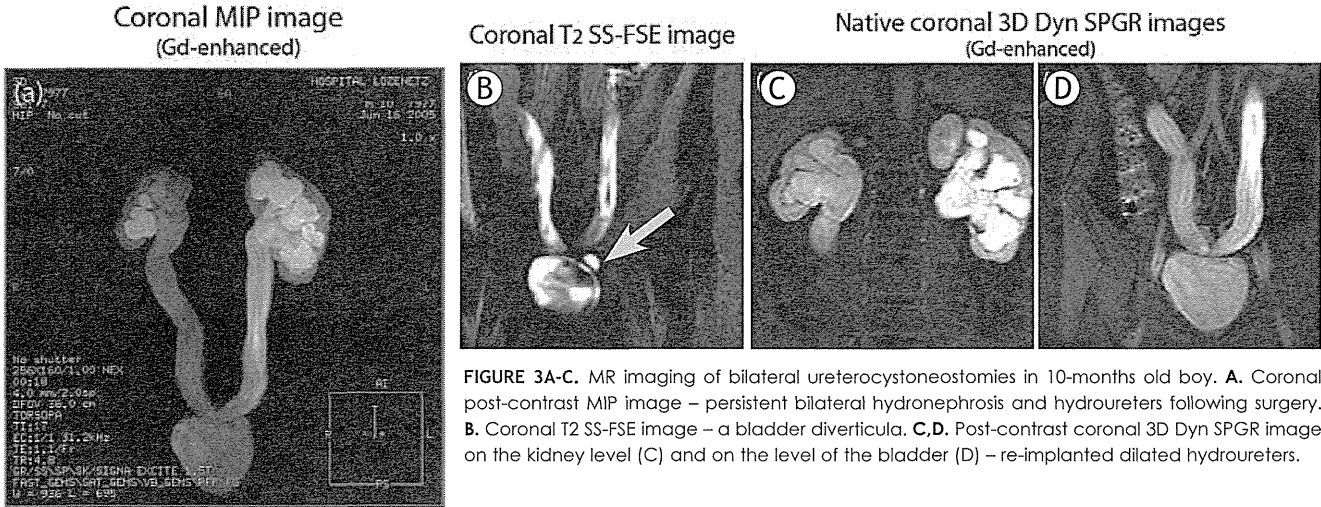## Statistical analysis and ethical consideration

Groups were compared with Mann-Whitney U-test, P-values >0.05 were taken as indicators of no statistically significant differences. SPSS 13.0 (SPSS Inc., Chicago, Illinois, USA) was used.

The investigators strictly followed recommendations of the Helsinki Declaration (1964, with later amendments) and of the European Council Convention on Protection of Human Rights in Bio-Medicine (Oviedo 1997).

Results

MR urography for visualization of morphological renal anomalies in children

Static, T2 MR urography was successfully performed in 96 children with 99 exams, totally 197 kidneys (in three children follow-up MRI exams after surgery have been done and in one patient left nephrectomy was performed). T2 images for anatomic evaluation were helpful in the assess-

Coronal MIP image
(Gd-enhanced)

Coronal T2 SS-FSE image

Native coronal 3D Dyn SPGR images
(Gd-enhanced)

FIGURE 3A-C. MR imaging of bilateral ureterocystoneostomies in 10-months old boy. **A.** Coronal post-contrast MIP image – persistent bilateral hydronephrosis and hydroureters following surgery. **B.** Coronal T2 SS-FSE image – a bladder diverticula. **C,D.** Post-contrast coronal 3D Dyn SPGR image on the kidney level (C) and on the level of the bladder (D) – re-implanted dilated hydroureters.

ment of children with severe hydronephrosis and poorly functioning systems. The majority of the population (91 cases) presented with congenital anomalies of the renal pelvis and ureter, including megacalycosis, ureteropelvic (UPJ) obstruction and primary megaureters. We also detected 36 cases of congenital anomalies of the kidney, including: renal agenesis – 6; renal hypoplasia – 5; cystic anomalies of the kidneys – 8; anomalies of renal rotation, horseshoe kidney – 6 (Figure 2); renal dystopia – 3; abnormal renal vessels – 6; Fraley's syndrome -2. Static, T2 MRU allows us also to find the following anomalies: (i) bladder anomalies – in 3 children; (ii) encountered lower urinary tract anomalies of urogenital sinus – in 7 children, including disorders of sex development with ambiguous genitalia (hermaphroditism) (n=3), anorectal and vaginal malformations (n=4); (iii) renal infections – in 18 children. 11 cases of renal neoplasms were confirmed or detected on MRU. In 13 cases, no abnormalities were detected on the static, T2 MR urography.

## MR urography for assessment of renal function in children

In 54 children (from the whole population), T1 excretory MR urography with injection of Gd has been performed in addition to static, T2 MR urography for the main purpose of our study – to assess the renal function. The majority of them had anomalies of the renal pelvis and ureter: ureteropelvic (UPJ) obstruction (hydronephrosis) – 43 (bilateral – 10, right side – 14, left side – 19); primary megaureter and anomalies of vesicoureteral segment (UVJ) – 30 (bilateral – 8, right side – 8, left side – 14) including 7 patients with vesicoureteric reflux

(VUR), diagnosed by VCUG, ureter duplication – 2; ureterocele – 2. We observed obstructed systems on MR urography morphologically by the presence of narrowed ureter with proximal dilatation and we were able to distinguish obstructed from non-obstructed systems functionally by the presence of delayed contrast excretion into the collecting system and ureter on the basis of the functional analysis in particular by the calculation of renal transit times (RTT). In 40 children MR functional analysis proved the presence of obstructive systems and the remaining 14 children were classified as non-obstructive and they have been followed-up. Both static and excretory MR urography was helpful in differentiating the causes of hydronephrosis in these patients. Typical images of a child with several bilateral ureterocystoneostomies and persistent bilateral hydronephrosis and hydroureters following surgery are shown in Figure 3.

We consider images quality of the kidney and the collecting system to be superior with MR urography in comparison to ultrasound and DTPA renogram in all 96 cases. The agreement of grading of hydronephrosis was equal in MR urography and ultrasound (US), however MR provides a detailed visualization of the entire ureters and presents ureteric pathology clearly US.

A correlation between MRU data and final diagnosis determined by surgery or observation was excellent in all 96 patients. 40 children benefits from surgical interventions for obstructive systems. Pyeloplasty has been performed in 11 with MR findings of ureteropelvic junction (UPJ) obstruction (Figure 4). In 29 children with UVJ obstruction and primary megaureter, reimplantation of the ureters - ureterocystoneostomy (UCNS) has been
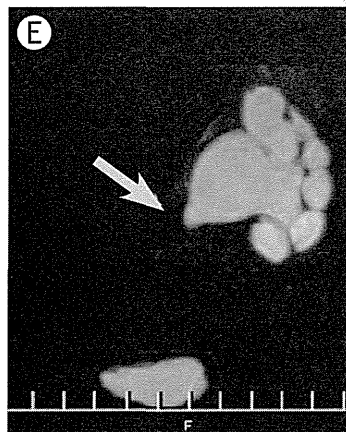
Coronal T1-weighted MRU (Gd-enhanced)
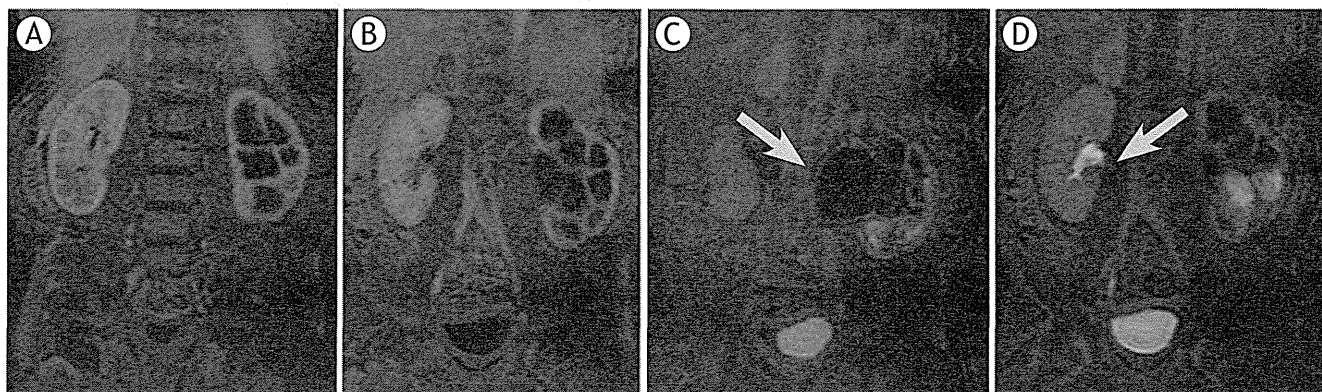
Scinfigraphy
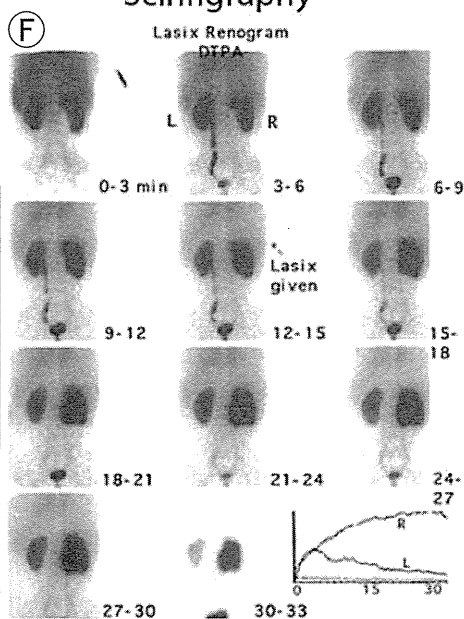
Coronal T2-weighted MIP image
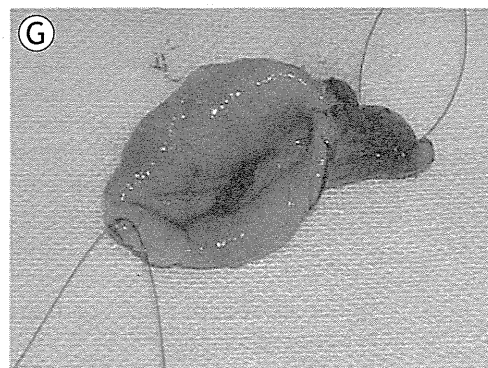
Post-operative pathologic specimen

FIGURE 4A-G. Imaging of UPJ obstruction in 9-month-old boy. **A-D.** Consecutive coronal T1-weighted MR images (Gd-enhanced) – successively filling of the right renal pelvis with preservation of the right kidney function. **E.** Coronal T2-weighted MIP image – on the left side an outflow tract obstruction with marked dilatation of the left pyelocalyceal system; **F.** Dynamic 99mTc-DTPA presenting urinary obstruction of the left kidney; **G.** Postoperative pathologic specimen in th same child following pyeloplasty a modo Anderson-Hynes.

performed (Figure 3). Other surgical interventions (74 in total for the whole study population), such as nephrectomies, partial or atypical kidney resection, nephrostomies, external genitalia corrections, masculinizing surgical procedures, retroperitoneal tumours resections etc. were also confirmed at MR urography.

VCUG was performed in 10 patients. Vesico-ureteric reflux (VUR) in 7 patients and in one case an ureterocele was identified. The vesico-ureteric reflux was classified as grade III in 4 children, grade IV in 2 and grade V in 1; in both cases pre-senting dilatation of the ureter and the pyelocalyceal system were clearly visible on MR urograms. In two cases VCUG present normal findings.

A comparison of the results from the functional analysis has been done by two different softwares – "CHOP-fMRU" and "ImageJ", as well as by the data from the 99mTc-DTPA. The results from the functional analysis of transit times, volumes and volumetric differential renal function are presented on Table 1. No statistically significant differences ($P>0.05$) were found between the calyceal and renal transit times and the parenchymal kidney

TABLE 1. Calculated transit times, parenchymal volumes and volumetric differential renal function

Transit times		Parenchymal volumes		Volumetric differential renal function			
CHOP-fMRU/ ImageJ	Time (range)	CHOP-fMRU/ ImageJ	Volume (range)	CHOP-fMRU/ ImageJ/NucMed	Percent (range)	SE	SD
CHOP-CTT-R	313 sec. (150-476)	CHOP-Volume-R	134,9 ml (14,3-255,6)	CHOP-vDRF-R	54,15% (44,18-64,11)	3,88	9,50
ImageJ-CTT-R	279 sec. (151-407)	ImageJ-Volume-R	129,2 ml (19,5-238,9)	CHOP-vDRF-L	48,85% (35,88-55,82)	3,88	9,50
CHOP-CTT-L	267 sec. (141-393)	CHOP-Volume-L	147,2 ml (12,4-282,0)	ImageJ-DRF-R	52,40% (44,60-60,20)	3,04	7,44
ImageJ-CTT-L	243 sec. (126-361)	ImageJ-Volume-L	150,3 ml (15,7-284,9)	ImageJ-DRF-L	47,60% (39,80-55,40)	3,04	7,44
CHOP-RTT-R	534 sec. (287-780)			NucMed-DRF-R	51,92% (47,27-56,56)	1,81	4,43
ImageJ-RTT-R	550 sec. (306-793)			NucMed-DRF-L	48,08% (43,44-52,73)	1,81	4,43
CHOP-RTT-L	476 sec. (290-663)						
ImageJ-RTT-L	475 sec. (277-673)5						

Legend: R = right kidney, L = left kidney; CHOP-CTT = mean calycial transit time measured with CHOP-fMRU; CHOP-RTT = mean renal transit time measured with CHOP-fMRU;, ImageJ-CTT - mean calycial transit time measured with ImageJ; ImageJ-RTT = mean renal transit time measured with ImageJ; CHOP-Volume and ImageJ-Volume = parenchymal volumes, measured with CHOP-fMRU and ImageJ; CHOP-vDRF, ImageJ-vDRF and NucMed-DRF = volumetric differential renal function, measured respir. with CHOP-fMRU, ImageJ and Nuclear Medicine; SE = standard error; SD = standard deviation.
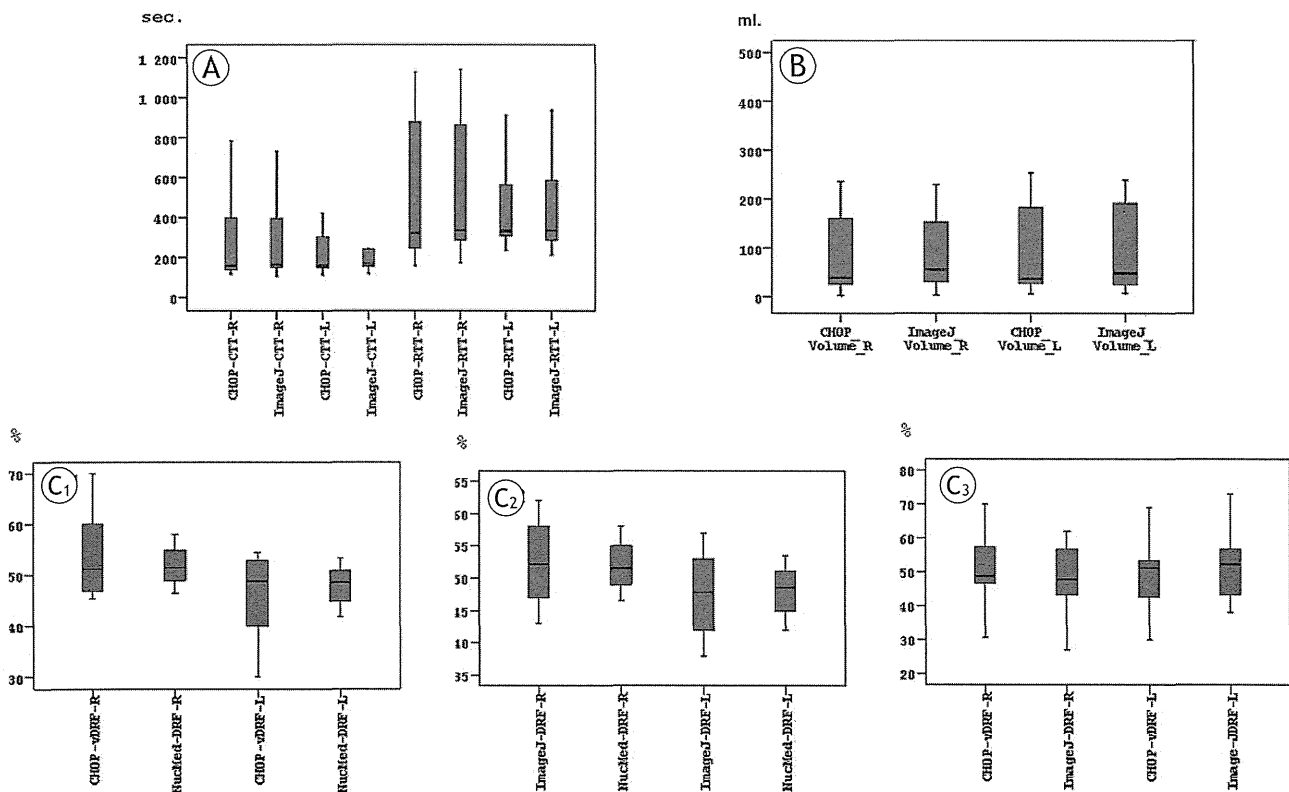

FIGURE 5A-C. Box-plots of different parameters for right and left kidney evaluated by CHOP-fMRU and ImageJ. A. cTT and rTT. B. Parenchymal volumes. C1,2,3. Volumetric differential renal function, as well as 99mTc-DTPA renal function.

Static coronal T2 SS-FSE MRU
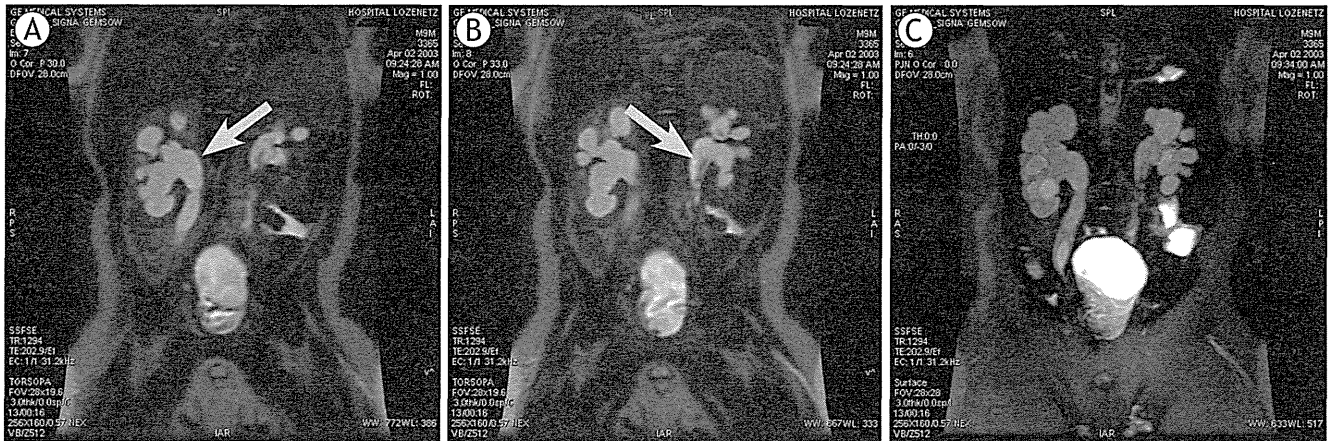
Coronal MIP image

FIGURE 6A-C. MR imaging of persistent bilateral hydronephrosis and hydroureters in 9-month old boy, following ureterocystoneostomy. **A,B.** Static coronal T2-weghted MR images using single-shot fast spin echo (SS-FSE). **C.** Coronal MIP image.

volumes, measured by CHOP-fMRU and ImageJ (Figure 5A,B). The values for the volumetric differential kidney function assessed by CHOP-fMRU and ImageJ measured separately for each kidney were not statistically different to those derived from the Tc-DTPA study (P>0.05) (Figure $5C_{1,2,3}$). MR urography and renal scintigraphy showed confirmatory results in the diagnosis of obstruction both UPJ and UVJ in terms of volumetric differential renal function values.

Discussion

MRU is a feasible method for evaluation of urinary tract pathology in neonates and infants.[1,16] It overcomes the limitations of the conventional imaging techniques and is superior tool in many aspects, especially in the evaluation of parenchymal kidney diseases and poorly functioning systems, assessment of ureteral anatomy and renal vasculature as shown in our study. The method is particularly helpful for further therapeutic decisions, planning of surgical intervention and future diagnostic work-up.

The most common MRU techniques, used to visualize the urinary tract, are the static (T_2) MRU and excretory (T_1) MRU.[17-19] Three-dimensional (3D) sequences are used to obtain thin-section data sets that can be further post-processed to create volume-rendered (VR) or maximum-intensity-projection (MIP) images of the entire urinary tract (Figure 6). Similar observations have been as reported by Roy et al. and O'Malley et al., using MRU.[20-21] Excretory

(T_1) MRU is similar to CT urography and intravenous urography. The use of dose of Gd (0.1 mmol/kg) and in some occasions low-dose Gd opacification (0.01 mmol/kg) allowed us to maintain the linearity between signal and Gd concentration, which is essential for quantitative measurements and analysis. Administration of diuretics improved the quality of MRU by increasing the quantity of the urine and therefore, leads to better dilution and appropriate distribution of Gd in the urinary tract.[22-23] The most important sequence of excretory MRU in our study was 3D gradient-echo. Fat-suppression is recommended for better demonstration of the ureters. Modern MR-units scan simultaneously in one volume the kidneys, the ureters and the bladder, using 3D gradient-echo sequences in one breath-hold.[19,24] Sometimes segmental scanning of the kidneys or bladder separately for visualization of image details is recommended.

Currently, there are two major MRU processing software available free of charge, which we have verified, compared each other and used in our practice routinely.[5,9] Post-processing algorithms permits us to evaluate and compare to scintigraphy several parameters – (i) calycial (cTT) and renal transit times (rTT); (ii) parenchymal volumes; (iii) differentiated renal function (vDRF) and (iv) the time-intensity curves representative for the renal function.

Our results demonstrate that MRU should be a method of choice for visualization of the upper urinary tract in children as it is difficult to assess by US or scintigraphy. In some cases, such as UPJ obstruction, MRU was confirmatory to ultrasound,
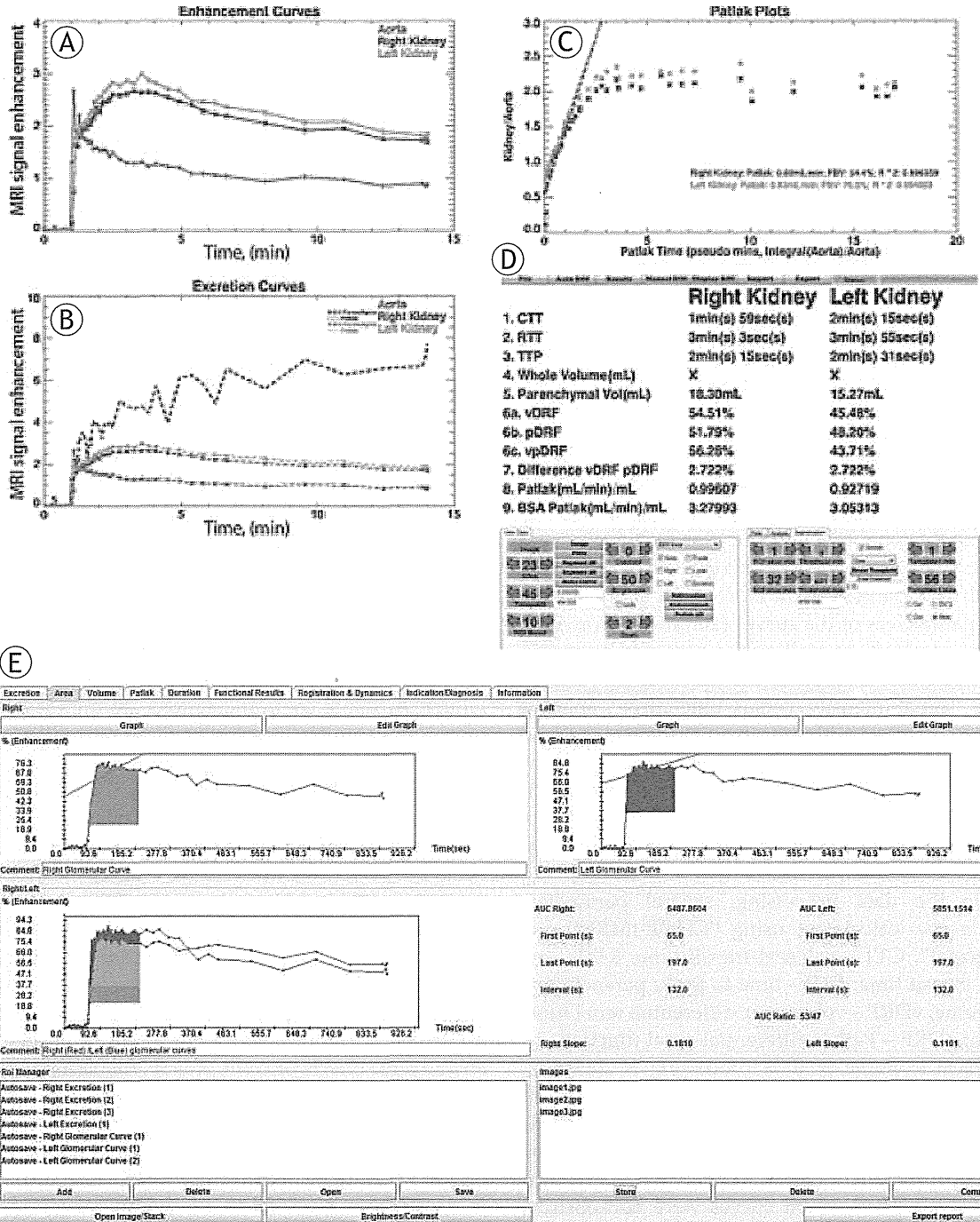
FIGURE 7A-E. Automated functional analysis of MRU data in bilateral normal kidney with vesicoureteral reflux(VUR) – grade 1 on the right side using "CHOP-fMRU". **A.** Enhancement curves. **B.** Excretion curves. **C.** Patlak plots. **D.** Calculation of renal transit times and differential renal function. **E.** Enhancement curves, generated on "ImageJ".

but superior concerning the evaluation of end-ureteral anomalies. US provides initial information concerning renal parenchyma, bladder morphology, presence and degree of dilated systems, but failed in visualization of non-accessible ureters, hidden in the retroperitoneum and is pretty week in information about renal excretion.

The graphic presentation of time-intensity curves, obtained by the dynamic MRU studies, was in accordance with the renal curves, obtained by scintigraphy. Moreover, the calculated values of the volumetric differential renal function, using "CHOP-fMRU" software were similar to those calculated on the basis of ImageJ software; both corresponded to the values from the dynamic 99mTc-DTPA scintigraphy. Comparable results regarding parenchymal volumes and transit times were observed using the two different software programs. Scintigraphy also supplies information about the renal function and morphology; however it is time-consuming ionizing imaging method with low spatial resolution.[6,25] In our study, the basic parameters of the curves (amplitude, washout) were assessed, as well as the presence of certain characteristic features of the curve. The data from the "signal-intensity versus time-curve" analysis were combined with the other parameters, derived from the MRU analysis, including estimation of the renal transit times, parenchymal volumes and differential renal function. The resulted data-set provided a powerful tool, of high importance for the diagnosis of obstruction.

In the data processing, several parameters were also calculated, using "CHOP-fMRU" and "ImageJ": CTT – calyceal transit time; RTsT – renal transit time; TTP – time to peak; parenchymal volume; vDRF – volumetric differential renal function; pDRF – Patlak differential renal function etc. Typical example of data processing is shown in Figure 7 – a child with recurrent renal infections and a low-grade vesicoureteral reflux (VUR) on the left side. On non-contrast MRU images dilatation of the distal part of the left ureter was observed, the resulting enhancement curves were non-obstructive and the patient was referred to ultrasonography follow-up. No significant difference concerning the listed parameters was found whatever functional analysis software has been used.

Our results as well as the presented case (Figure 7) showed that both renal and calycial transit times, parenchymal volumes and differential renal function are indicators for kidney dysfunction.

Even small functional disorders can be detected using MRU and analysing these parameters. The complex software functional analysis of the whole patient population confirmed this assumption.

In addition to the advantages of MRU, mentioned above, it is necessary to note that this technique has also some limitations. Sometimes it requires a placement of bladder catheter, administration of furosemide and Gd, sedation and even anaesthesia (for newborns and younger children), as a complementary risk. Breath-hold techniques could not be applied in neonates and small infants and motion artefacts should be at a minimum. Patient preparation and examination itself are time-consuming; post-processing and calculation of functional curves and differential renal function requires additional time.

In 2006, it was demonstrated that some Gd-based contrast agents may provoke the development of nephrogenic systemic fibrosis (NSF) and/or a generalized fibrotic disorder in renal failure patients.[26] Gd-ions, released from Gd-based MR contrast agents, are the likely etiologic agent of NSF.[27] The ESUR guidelines suggest a very careful administration of Gd in children with renal failure. Absolute contraindications are high levels of creatinine and a glomerular filtration under 30 ml/min/1.73 m². Individual assessment for the indications and the need of contrast-enhanced MR examination was performed after discussions with paediatric nephrologists in cases of glomerular filtration between 30 and 60 ml/min/1.73 m². Written consent should be obtained in spite of the fact that most cases of NSF occurs in adults and the reported cases of NSF without Gd administration. In all patients with high risk for development of NSF and in the paediatric group, we used cyclic Gd-helators due to their higher stability.[28] We didn't observe any adverse effects or cases of NSF, following contrast administration in our study-group.

In conclusion, MR urography is useful, non-ionizing method for assessment of obstructive uropathies and facilitates surgical decisions. There is growing number of publications concerning the criteria for assessment of the renal function in children by dynamic MRU, but the achievement of consensus requires more and deeper investigations. The advances of molecular imaging techniques provide new insights about the nature of hereditary diseases in paediatric nephrology and urology.

References

1. Vegar-Zubovic S, Kristic S, Lincender L. Magnetic resonance urography in children - when and why? *Radiol Oncol* 2011; **45:** 174-9.

2. Miklos M, Gajski G, Garaj-Vrhovac V. Usage of the standard and modified comet assay in assessment of DNA damage in human lymphocytes after exposure to ionizing radiation. *Radiol Oncol* 2009; **43:** 97-107.

3. Apaydin M, Varer M, Oztekin O. Radiological considerations in von Hippel-Lindeau disease: imaging findings and the review of the literature. *Radiol Oncol* 2010; **44:** 164-7.

4. Kachanov DY, Dobrenkov KV, Shamanskaya TV, Abdullaev RT, Inushkina EV, Savkova RF, et al. Solid tumors in young children in Moscow Region of Russian Federation. *Radiol Oncol* 2008; **42:** 39-44.

5. Khrichenko D, Darge K. Functional analysis in MR urography – made simple. *Pediatr Radiol* 2010; **40:** 182-99.

6. Avni EF, Bali MA, Regnault M, Damry N, Degroot F, Metens T, et al. MR urography in children. *Eur J Radiol* 2002; **43:** 154-66.

7. Grattan-Smith JD, Jones RA. MR urography in children. *Pediatr Radiol* 2006; **36:** 1119-32; quiz 228-9.

8. Vivier PH, Blondiaux E, Dolores M, Marouteau-Pasquier N, Brasseur M, Petitjean C, et al. [Functional MR urography in children]. [French]. *Journal de Radiologie* 2009; **90:** 11-9.

9. Vivier PH, Dolores M, Taylor M, Dacher JN. MR urography in children. Part 2: how to use ImageJ MR urography processing software. *Pediatr Radiol* 2010; **40:** 739-46.

10. Grattan-Smith JD, Little SB, Jones RA. MR urography in children: how we do it. *Pediatr Radiol* 2008; 38 Suppl **1:** S3-17.

11. Leyendecker JR, Barnes CE, Zagoria RJ. MR urography: techniques and clinical applications. *Radiographics* 2008; **28:** 23-46; 46-7.

12. Grattan-Smith JD, Perez-Bayfield MR, Jones RA, Little S, Broecker B, Smith EA, et al. MR imaging of kidneys: functional evaluation using F-15 perfusion imaging. *Pediatr Radiol* 2003; **33:** 293-304.

13. Cengiz M, Baysal Z, Ganidagli S. Oral sedation with midazolam and diphenhydramine compared with midazolam alone in children undergoing magnetic resonance imaging. *Paediatr Anaesth* 2006; **16:** 621-6.

14. Lin TF, Yeh YC, Yen YH, Wang YP, Lin CJ, Sun WZ. Antiemetic and analgesic-sparing effects of diphenhydramine added to morphine intravenous patient-controlled analgesia. *Br J Anaesth* 2005; **94:** 835-9.

15. Ring E, Riccabona M, Fotter R. Normal values: pediatric uroradiology. Berlin: Springer; 2008. p. 507-14.

16. Riccabona M, Simbrunner J, Ring E, Ruppert-Kohlmayr A, Ebner F, Fotter R. Feasibility of MR urography in neonates and infants with anomalies of the upper urinary tract. *Eur Radiol* 2002; **12:** 1442-50.

17. Nolte-Ernsting CC, Staatz G, Tacke J, Gunther RW. MR urography today. *Abdom Imaging* 2003; 28: 191-209.

18. Garcia-Valtuille R, Garcia-Valtuille AI, Abascal F, Cerezal L, Arguello MC. Magnetic resonance urography: a pictorial overview. *Br J Radiol* 2006; **79:** 614-26.

19. Nolte-Ernsting CC, Adam GB, Gunther RW. MR urography: examination techniques and clinical applications. *Eur Radiol* 2001; **11:** 355-72.

20. Roy C, Saussine C, Guth S, Horviller S, Tuchmann C, Vasilescu C, et al. MR urography in the evaluation of urinary tract obstruction. *Abdom Imaging* 1998; **23:** 27-34.

21. O'Malley ME, Soto JA, Yucel EK, Hussain S. MR urography: evaluation of a three-dimensional fast spin-echo technique in patients with hydronephrosis. *AJR Am J Roentgenol* 1997; **168:** 387-92.

22. Szopinski K, Szopinska M, Borowka A, Jakubowski W. Magnetic resonance urography: initial experience of a low-dose Gd-DTPA-enhanced technique. *Eur Radiol* 2000; **10:** 1158-64.

23. Hughes J, Jan W, Goodie J, Lund R, Rankin S. MR urography: evaluation of different techniques in non-dilated tracts. *Clin Radiol* 2002; **57:** 989-94.

24. Sudah M, Vanninen R, Partanen K, Heino A, Vainio P, Ala-Opas M. MR urography in evaluation of acute flank pain: T2-weighted sequences and gadolinium-enhanced three-dimensional FLASH compared with urography. Fast low-angle shot. *AJR Am J Roentgenol* 2001; **176:** 105-12.

25. Borthne A, Pierre-Jerome C, Nordshus T, Reiseter T. MR urography in children: current status and future development. *Eur Radiol* 2000; **10:** 503-11.

26. Thomsen HS, Marckmann P. Extracellular Gd-CA: differences in prevalence of NSF. *Eur J Radiol* 2008; **66:** 180-3.

27. Abraham JL, Thakral C, Skov L, Rossen K, Marckmann P. Dermal inorganic gadolinium concentrations: evidence for in vivo transmetallation and long-term persistence in nephrogenic systemic fibrosis. *Br J Dermatol* 2008; **158:** 273-80.

28. Martin DR, Sharma P, Salman K, Jones RA, Grattan-Smith JD, Mao H, et al. Individual kidney blood flow measured with contrast-enhanced first-pass perfusion MR imaging. *Radiology* 2008; **246:** 241-8.

科学技術・大学

有機化合物の磁性

立体構造解析で証明

磁性を持つ抗がん剤

横浜市大とIHI

横浜市立大学大学院医学研究科の石川義弘教授とIHIのグループは、磁性を持つ抗がん剤の分子構造を解析することに成功した。分子構造から、抗がん剤自体が磁性を持つことが証明できたという。

同抗がん剤はグループが6-7年前に開発。投与後に外部から磁場を当てて腫瘍部に抗がん剤を集中させることで、効果的にがん細胞を攻撃できる。現在は動物での実証実験を進めており、分子構造が解明できたことで、実用化への前進が期待される。

磁性機能の裏付けをした抗がん剤

を持つ詳しい理由は不明だった。今回、抗がん剤成分の分子を濃縮して結晶化、X線で構造を解析した。その結果から、分子の立体構造によって磁性が生じる理由が説明できたという。

外部から磁場を当てて抗がん剤をがん組織に集められることから、皮膚がんや舌がんなど体の表面にできるがんへの応用が期待される。これまでにマウスやウサギを使った実験で、磁場を当てない場合に比べて2倍以上の治療効果を引き出せることを確認している。また、肺裏面の薄い膜であるがん胸膜にできる悪性中皮腫など、外科手術での切除の難しいがんに応用できる可能性もある。

さらに交流磁場を加えることで、体内に投与した抗がん剤にうず電流を生じさせ、発熱させることもできる。グループでは、がん細胞を温めて死滅させる温熱療法への応用も、検討しているという。

率的に探索するIHIの技術を応用し、抗がん作用を持つさまざまな物質の中から常温で磁性を持つものを見つけていた。

同抗がん剤は有機化合物で、鉄などの金属は含まない。これまで、磁性を持つ抗がん剤

グループは開発していた抗がん剤に「EI-236」というコード名を付けている。磁性材料を効